Cell Reports
Physical Science

CellPress
OPEN ACCESS

Article

Flexible amino acid-based energy harvesting for structural health monitoring of water pipes

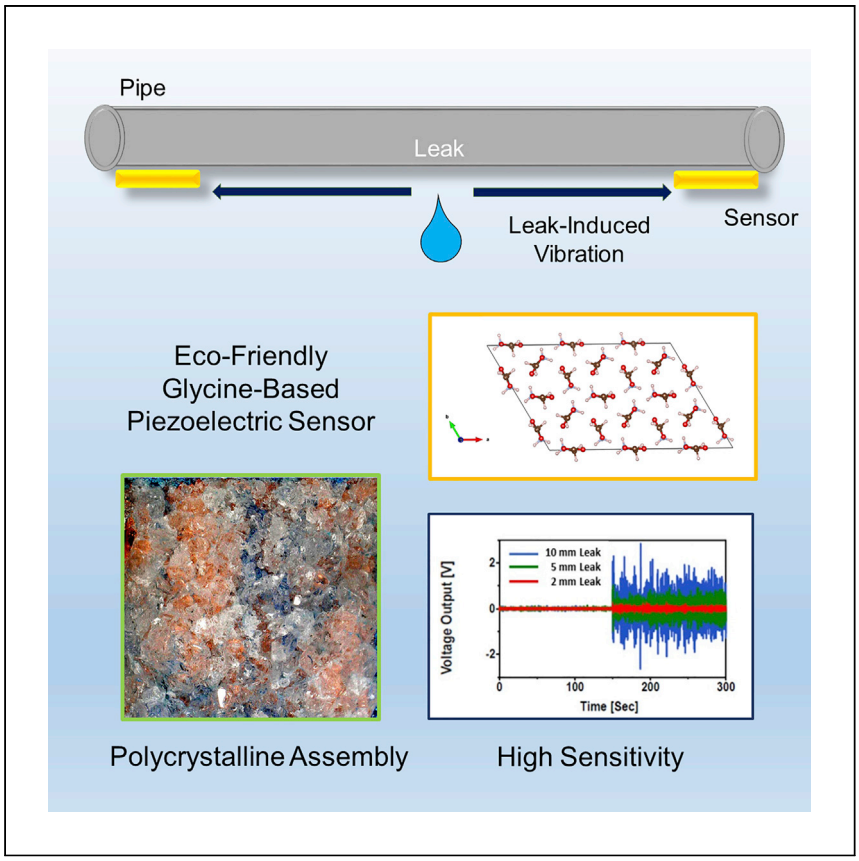

Commercial piezoelectric sensors are a ubiquitous part of modern-day technologies but rely on materials that are damaging to the environment. Okosun et al. have validated a low-cost, eco-friendly piezoelectric sensor as a structural health monitor that can detect leakage in water pipes, outperforming lead-based ceramics and organic polymers.

Favour Okosun, Sarah Guerin, Mert Celikin, Vikram Pakrashi

sarah.guerin@ul.ie

Highlights

Glycine crystals grown as a high-concentration, polycrystalline piezoelectric sensor

High-performance device validated for structural health monitoring of pipe damage

Low-dielectric material demonstrates consistently higher sensitivity than PVDF

Low-cost, eco-friendly material capable of data-driven decision making

Okosun et al., Cell Reports Physical Science 2, 100434
May 19, 2021
https://doi.org/10.1016/j.xcrp.2021.100434

Cell Reports
Physical Science

CellPress
OPEN ACCESS

Article

Flexible amino acid-based energy harvesting for structural health monitoring of water pipes

Favour Okosun,[1,2,3,8] Sarah Guerin,[4,5,9,12,*] Mert Celikin,[6,7,10] and Vikram Pakrashi[1,2,3,11]

SUMMARY

Biomolecular piezoelectric materials offer an inexpensive, non-toxic, and renewable alternative to current commercial piezoelectrics, which rely on toxic heavy elements. Currently, there is a lack of testing for real-world applications of these eco-friendly crystals. Here, we validate an amino acid-based sensor capable of real-time detection of pipe leakage, a global challenge for sustainable water access. The polycrystalline device demonstrates data-driven decision making in identifying degraded pipelines, exploiting the relationship between leak-induced vibration and piezoelectric voltage. The device has piezoelectric strain and voltage constants of 0.9 pC/N and 60 mV m/N. Peak voltage of ~2 V is recorded in the low-dielectric film at high flow rates and large leak size. The glycine crystal sensors demonstrate much higher sensitivity than PVDF polymer patches. The sensors can operate over a range of test leak sizes, with the energy content of the worst leak state being >10 times that of a healthy pipe.

INTRODUCTION

In the past 10 years, biological piezoelectric materials have emerged as the potential next generation of cost-effective, green electromechanical sensors.[1–3] The piezoelectric voltages produced under an applied force are inversely proportional to the dielectric constant of the material, and so even "weak" organic piezoelectrics (with modest piezoelectric constants compared to inorganic ceramics[4,5]) can generate large voltages in response to strain. Amino acids are the simplest biological units, are inexpensive and easy to crystallize,[6–9] and demonstrate measurable piezoelectricity in single crystal[10–12] and polycrystalline forms.[13,14] The γ-glycine polymorph in the present study is the only amino acid crystal with 3 finite longitudinal piezoelectric constants in single crystal form,[10] ranging from 1 to 10 pC/N. Its electromechanical properties are highly stable at room temperature, and as we demonstrate, the crystal solution is suitable for batch processing on flexible conductive substrates. γ-glycine is a stable polymorph under high humidity, with metastable polymorphs transforming into the γ form as humidity increases.[15]

Leak detection in fluid-carrying pipes is crucial for sustainable water access, and vibration-based techniques have proven to be effective at early detection of leak onset.[16–19] Current commercial solutions are either battery powered,[20–22] or, if piezoelectric, very costly.[23,24] In addition, most commercial accelerometers have rigid structures,[25] making them unsuitable for bonding to curved pipes. Alternative patch-type piezoelectric sensors have proven effective for pipe leak detection and monitoring,[26] fabricated from commercially procured polyvinylidene difluoride (PVDF) films despite the complex high-temperature synthesis and electric poling requirements.[27,28] A central focus of this article is the growing of alternative organic

[1]Dynamical Systems and Risk Laboratory, School of Mechanical and Materials Engineering, University College Dublin, Dublin D04 V1W8, Ireland

[2]Science Foundation Ireland (SFI) MaREI Centre, University College Dublin, Dublin, Ireland

[3]The Energy Institute, University College Dublin, Dublin D04 V1W8, Ireland

[4]Department of Physics, Bernal Institute, University of Limerick, Limerick V94 T9PX, Ireland

[5]SSPC, Science Foundation Ireland Research Centre for Pharmaceuticals, University of Limerick, Limerick V94 T9PX, Ireland

[6]Materials Design and Processing Laboratory, School of Mechanical and Materials Engineering, University College Dublin, Dublin D04 V1W8, Ireland

[7]I-Form, the SFI Research Centre for Advanced Manufacturing, University College Dublin, Dublin D04 V1W8, Ireland

[8]Twitter: @Favour_Osose

[9]Twitter: @SPGuerin

[10]Twitter: @Mcelikin

[11]Twitter: @DSRL_UCDMECH

[12]Lead contact

*Correspondence: sarah.guerin@ul.ie

https://doi.org/10.1016/j.xcrp.2021.100434

glycine crystals on a flexible substrate and the subsequent fabrication of the biomolecular crystal assemblies into bio-based piezoelectric patches. This fabrication process requires far less experimental and environmental resources when compared to those of PVDF films.

Vibration-based techniques for pipe leak monitoring rely on both the fluid-structure interaction (FSI) and the negative pressure wave propagation attenuation mechanism (NPWPAM) phenomenon that propagates to the pipe surface and excites vibratory oscillations.[29–34] This works by bonding vibration sensors onto the outer pipe surface and measuring their electrical output due to the consequent pipe surface strain or acceleration due to this vibration.[35–37] For the healthy pipe state, the flow-induced vibration is due to FSI, and its magnitude is directly proportional to the fluid flow rate.[38,39] The onset of a pipe leak results in the generation of an additional NPW that decays away from the leak site equally in both directions,[40,41] creating an increase in pipe surface vibration levels as it propagates along sections of the pipe before dissipating. Baseline vibration signatures of a healthy pipe can be established from the bonded sensors and leaks can then be detected from an increase in signal amplitude over time. In a piezoelectric patch sensor, the generated charge is directly proportional to the pipe strain; therefore, the increased pipe vibration levels due to a leak result in increased amplitude of the sensor output voltage signal when compared to the baseline signal of the healthy pipe at the same flow rate. Details regarding FSI and NPWPAM and a summary of the derivation of their expressions is presented in Notes S1–S4, including Figures S1 and S2.

In this work, we experimentally validate flexible glycine-based sensors for pipe leak detection and monitoring in real time for a variety of flow rates and leak sizes using a custom fluid test rig developed for the validation of PVDF patches.[26] This is the first time that glycine crystals have been grown and characterized as a high-concentration, polycrystalline aggregate for piezoelectric sensing. We demonstrate that the sensors can detect the presence of a leak, localize the leak, and estimate the leak severity based on the voltage profile generated by the pipe vibration. The study demonstrates that low-dielectric, non-centrosymmetric biomolecular crystal films can work efficiently and sustainably as sensors for pipe structural health monitoring (SHM) applications, highlighting their potential in extensive monitoring of built infrastructure systems.

RESULTS AND DISCUSSION

Polycrystalline film growth and characterization

γ-Glycine crystallizes in a trigonal space group, endowing it with unique piezoelectric properties (Figure 1A). The orientation of the zwitterionic glycine molecules in the unit cell results in a net polarization along the crystallographic *c* axis at equilibrium, corresponding to a dipole of 14 D. What is unique about γ-glycine is that when a force is applied parallel to any crystallographic axis, a net polarization results along the same axis. When drop cast onto a flexible copper substrate at room temperature, the glycine solution evaporates to form a continuous polycrystalline film of randomly oriented crystal clusters (Figure 1B). If evaporation occurs below 283 K, glycine grows as sparse single crystals on the copper substrate, which are not suitable for device formation. Due to the random orientation of the crystals within the film, the effective piezoelectric response is lower than that of single crystals, and there is a higher standard deviation between films. Each crystal in the film will have an induced dipole along any of the 3 longitudinal axes when a mechanical stimulus is applied to that axis, with the bulk response of the device being the net surface

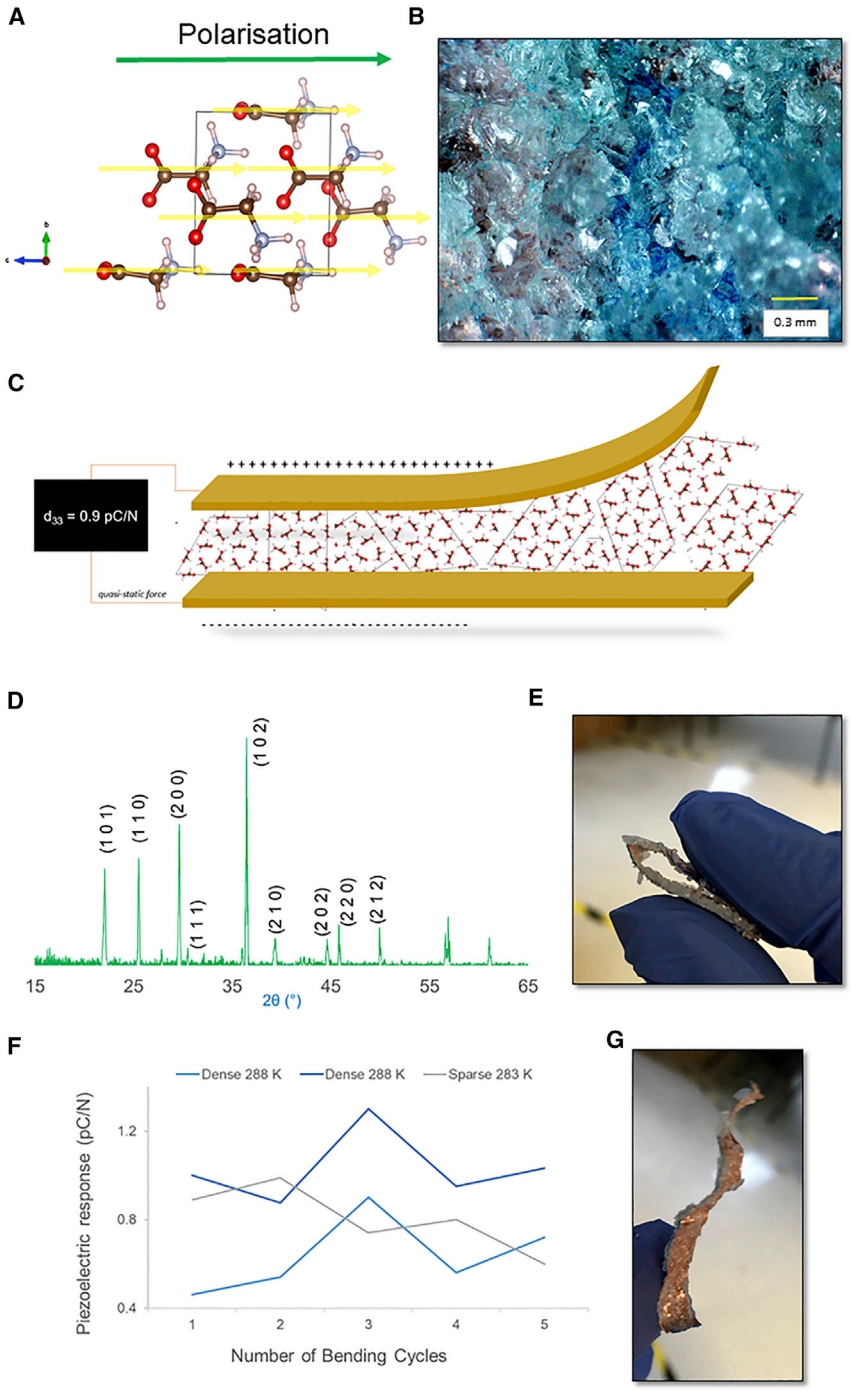

Figure 1. Characterization of bio-piezoelectric leak-detectors

(A) Crystal structure of γ-glycine, which allows for 3 longitudinal piezoelectric constants. Molecular dipoles are shown in yellow; the unit cell dipole is shown in green.

(B) Optical micrograph of the dense polycrystalline film.

(C) Device schematic showing randomly oriented γ-glycine clusters between 2 electrodes during piezoelectric characterization. The longitudinal piezoelectric surface charge generated during piezoelectric testing is also shown.

(D) XRD spectrum for a polycrystalline γ-glycine film with indexed peaks.

(E) A fully bent flexible glycine-based device.

(F) Graph of longitudinal d_{33} response for 3 devices over repeated bending and clamping cycles.

(G) Full-length view of the flexible polycrystalline active layer on copper tape.

Table 1. Material properties of the glycine sensors

Parameter	Value
Area, A_p	150 mm^2
Capacitance, C_p	28 pF
Thickness, t_p	80 μm
Modulus of elasticity, Y	28 GPa
Piezoelectric strain constant, d_{33}	0.9 pC/N
Piezoelectric voltage constant, g_{33}	60 mV m/N
Maximum longitudinal force	18 N
Maximum longitudinal pressure	57 kPa

Dimensions and physical properties of the polycrystalline device measured before fluid rig testing.

charge from each individual crystal (Figure 1C). X-ray diffraction (XRD) analysis shows excellent agreement in peak locations when compared to single crystal measurements.[6,42] For the polycrystalline films, the predominant peak corresponds to the (102) plane, followed in relative intensity by the (200) plane and the (110) plane (Figure 1D). When measured using the Berlincourt method, the effective longitudinal response d_{33} of the active crystal layer varied between 0.5 and 1.2 pC/N. To test the repeatability of the piezoelectric response, the glycine/copper films were tested after multiple cycles of bending the substrate (Figure 1E) and clamping under a 10-N force for measurement. Only the sparse films grown below 283 K showed a decrease in piezoelectric response (Figure 1F). The dense polycrystalline aggregates with a crystallite size of ~0.5 mm in diameter grown at 288 K showed a slight increase in piezoelectric response after repeated bending and clamping. While the crystals themselves are rigid, the individual crystallite size relative to the flexible substrate allows for a large range of motion of the whole device (Figure 1G). Furthermore, a piezoelectric material will only produce continuous sustained output to dynamic loading (strain/stress). If bending does not affect the properties, as shown here, then the initial bending-induced charge will decay quickly, and the output of the sensor should be zero when bonded to the pipe with no flow excitation. This was observed during the experiments as the sensors consistently recorded zero output when connected to the measuring chain before the start of the tests. Hence, the bonding of the sensor on the pipe does not affect the quality of the recorded signal output.

Given that the sensing mode for leak detection is vibration due to the leak-induced NPW propagation (which is generally low level in nature), the sensor will undergo neither extreme bending nor direct application of force during detection and measurement. To highlight the versatility and strength of the sensor, however, we quantify a fracturing force of 18 N, corresponding to an applied pressure of 57 kPa. When sealed with insulating tape and left in water for 24 h, the crystals show no signs of degradation and maintain their bulk piezo-response.

Three glycine sensors with identical longitudinal piezoelectric constants, $d_{33,}$ of 0.9 pC/N were chosen for testing in a flexible fluid test rig (Figure 1D). The physical properties of the glycine device (i.e., the polycrystalline film and flexible copper electrodes), are shown in Table 1, and the 3 glycine sensor patches are henceforth referred to as GS1, GS2, and GS3. Of particular note is the piezoelectric voltage constant, g_{33}, of 60 mV m/N, which exceeds that of commercial piezoelectric lead zirconium titanate (PZT).[43] This is due to the low-dielectric constant of the active layer, a property that has been engineered into piezoelectric ceramics such as barium titanate ($BaTiO_3$) via the introduction of a porous sandwich layer.[44]

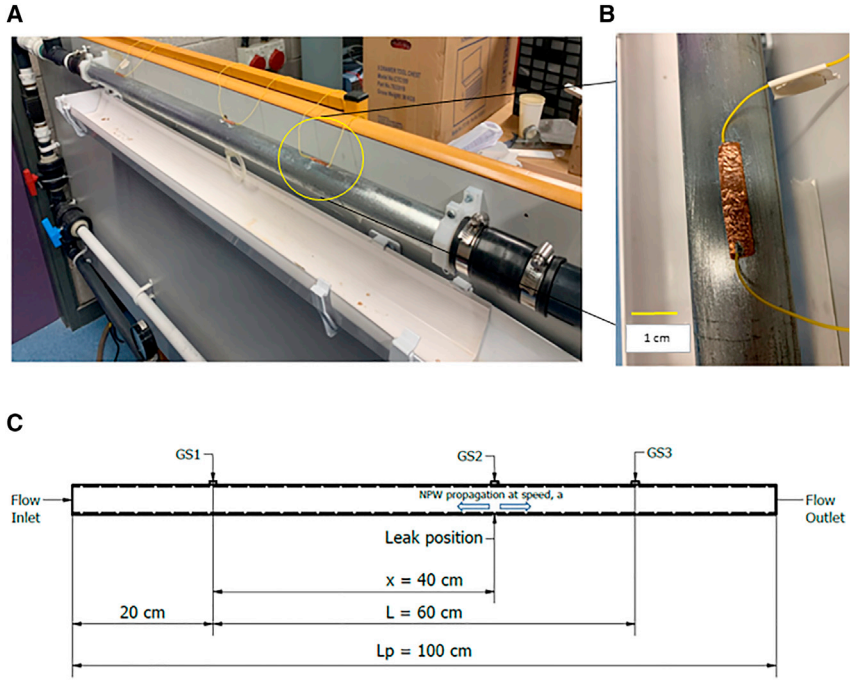

Figure 2. Measurement system and detection mechanism

(A) Fluid test rig with 3 glycine sensors (GS1, GS2, and GS3) attached.

(B) Close-up image of a sealed glycine sensor attached to the pipe test rig.

(C) Schematic of the fluid test rig showing vibration sensor location and NPW propagation parameters.

The fluid test rig shown in Figure 2A contains a fixed piping network and a flexible test pipe section. The test pipe is a 1-m galvanized steel pipe (see Table S1 for properties). The 3 glycine sensors were bonded to the outside of the test pipe (Figure 2B) at distances of 20, 60, and 80 cm past the test pipe inlet. Leak holes of diameter from 2 mm up to 10 mm were drilled at the 60-cm mark (the position of GS2). As such, GS1 is 40 cm upstream and GS3 is 20 cm downstream of the leak position (Figure 2C). These positions were selected to see how the time series data produced by each sensor reflects the attenuation of the leak-induced NPW to identify the location of the leak. To obtain comparative profiles for damaged and healthy pipes, custom fabricated leak plugs were used to seal the leak holes and restore the healthy state (HS) of the pipe (Figure S3). The leak plugs are then pulled out to model real-time introduction of the leaks.

Leak detection and monitoring

Figure 3 compares signals from the glycine patches for the healthy and damaged pipe states at different water flow rates. It can be deduced from the plots that a leak plug restores the non-leak state (LS) of the pipe, as the first half of the sensor voltage signal output (when the leak hole was still plugged) is a close match to that of the healthy pipe. Leak-induced additional pipe surface vibration gives a corresponding increase in the amplitudes of the voltage signals (at 150 s, data plotted in blue in Figure 3) from all three sensors bonded at different distances from the leak. This abrupt change in voltage is absent in the healthy pipe state (Figure 3, data in red), indicating that the leak-induced NPW propagates to all three regions of the pipe where the sensors are bonded before its complete decay. The fabricated glycine patch sensors can locate and assess the magnitude of the leak in real time

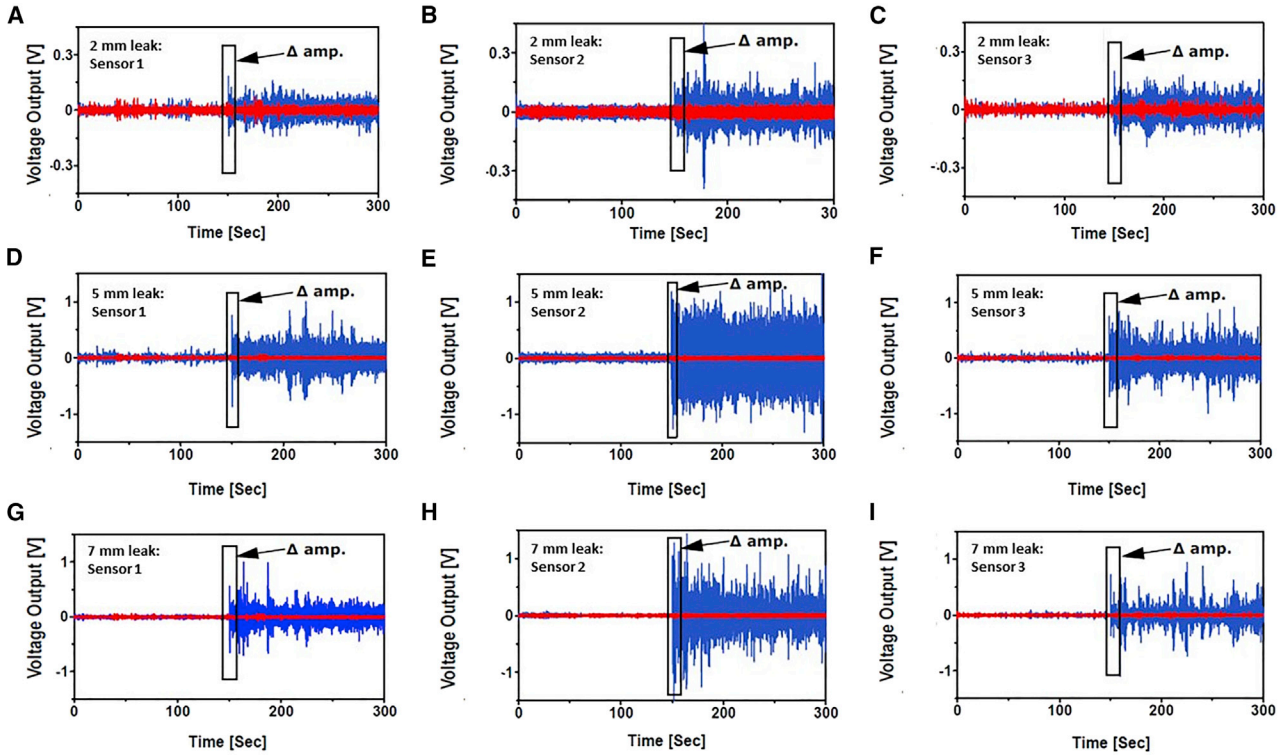

Figure 3. Sensor detection of individual leaks

(A–C) Voltage time plots for several test scenarios showing an increase in magnitude for individual sensor outputs for leak pipe states (blue) when compared to the corresponding healthy pipe states (red) at a common flow rate. Output is shown for a leak size of 2 mm at a flow rate of 26.50 L/min for (A) GS1, (B) GS2, and (C) GS3.

(D–F) Next shown are data for a 5-mm leak size at a flow rate of 90.85 L/min for (D) GS1, (E) GS2, and (F) GS3.

(G–I) The voltage output over time for a 7-mm leak size at a flow rate of 45.42 L/min is shown for (G) GS1, (H) GS2, and (I) GS3.

The label Δ amp. in the plots marks the leak-induced jump in signal amplitude.

by detecting the additional vibration caused by the leak. This is true for even the smallest leak size (2 mm diameter) at the lowest flow rate (26.50 L/min), as shown in Figures 3A–3C.

The magnitude of the NPW is directly proportional to the leak flow rate, which is in turn dependent on the leak size (Note S1). Consequently, the larger the leak size, the larger the leak-induced NPW and additional pipe surface vibration due to the leak. To validate this principle for real-time leak monitoring, we can examine the output from all three sensors at test scenarios with a common flow rate but varying leak sizes (Figure 4). The plots for GS1, GS2, and GS3 shown in Figures 4A–4C compare 3 signals from pipes with leak sizes of 2, 5, and 10 mm in diameter, all at a flow rate of 90.85 L/min (24 gpm [gallons per minute]). Larger voltage signals are recorded with larger leaks for all patch sensors and flow rates, demonstrating the dependence of the magnitude of the induced NPW on the leak size.

The output signal profiles in Figure 4 also show that the size of the NPW-induced step change grows with increasing leak size. The additional pipe surface vibration generated due to the introduction of a leak at a test flow rate of 45.42 L/min (Figures 4D–4F) scales with the diameter of the leak for all 3 sensors. This demonstrates that the fabricated glycine patch sensor can monitor a worsening pipe leak condition over time.

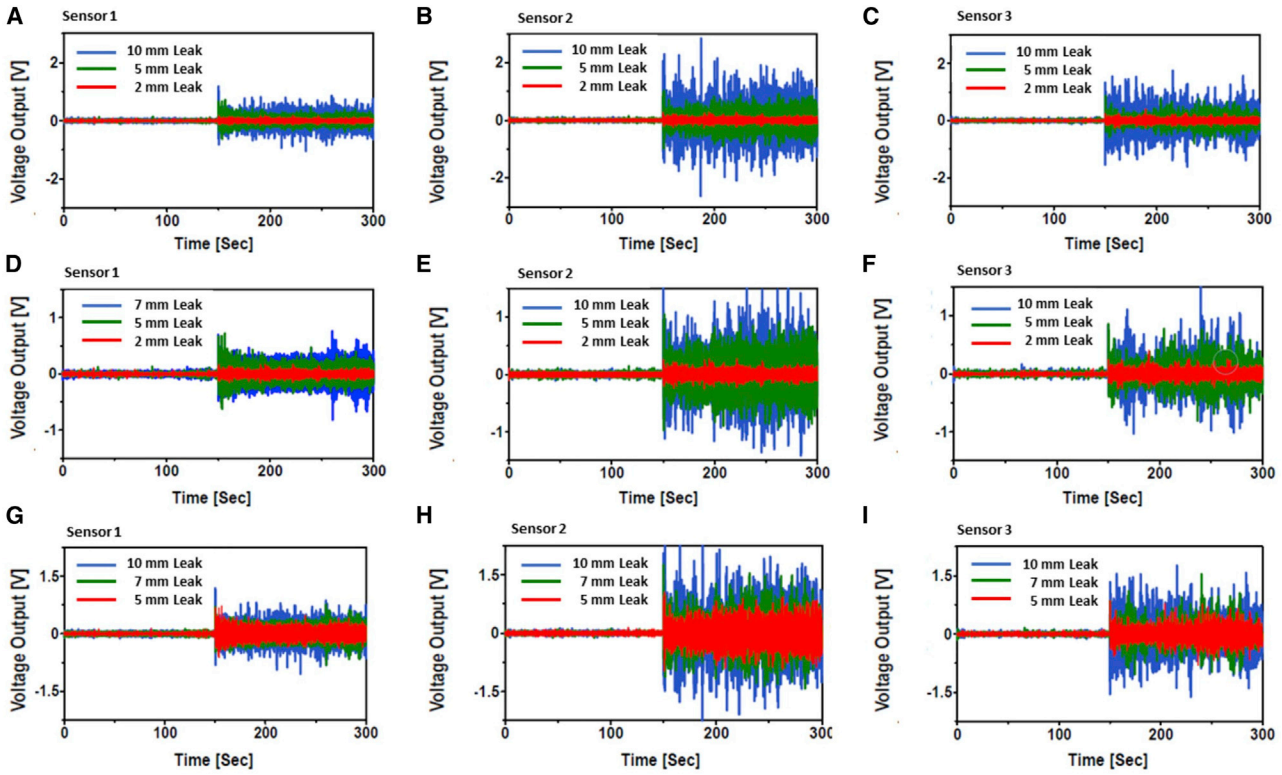

Figure 4. Identifying and distinguishing leak severity

Voltage time plots for several leak test scenarios showing consistent increase in individual sensor outputs for increasingly large leak states at same test flow rates. Output is shown for various leak sizes created at 150 s in pipes, with flow rate of 90.85 L/min in (A)–(C), 45.42 L/min in (D)–(F), and 71.92 L/min, in (G)–(I) for patch sensors GS1, GS2, and GS3, respectively.

To quantify the sensitivity of the glycine sensors over the range of test conditions (pipe states and flow rates), the increase in the energy content of the sensors' output due to the instantaneous introduction of a leak was quantified and expressed in terms of a leak index. Here, the recorded signal for each test scenario was divided into the healthy pipe section and the leak pipe section of the signal by identifying the point of abrupt change in the signal (~2.5 min, i.e., midway into the experiment). The energy content, in the form of the root mean square (RMS) voltage, of the sections was then calculated. The difference between the RMS voltage values of the sections (i.e., HS and LS sections) of each scenario quantifies the change in the sensor output due to the instantaneous introduction of leak midway through the experiment. The ratio of this difference and the HS RMS voltage value gives the deviation from the HS output due to the leak, and it is expressed here as the leak index. Table 2 presents leak index values for test scenarios involving the highest test flow rate and for all three glycine sensors.

Table 2 shows that a non-zero value of leak index is calculated for all LSs at 90.85 L/min. Also, the leak index calculated for GS2 at all LSs is the highest, which is expected because it is the sensor bonded directly above the leak. The highest leak index in this case is that of the highest flow rate and the worse LS test scenario (i.e., 10 mm LS and 90.85 L/min), which records an increase just over 10 times the voltage RMS of the healthy pipe state at that flow rate.

Table 2. Sensitivity of the amino acid-based sensor

	Leak index, 90.85 L/min		
Pipe state	GS1	GS2	GS3
HS	0	0	0
2.0 mm LS	0.33	2.24	1.04
5.0 mm LS	0.84	5.64	2.45
7.0 mm LS	1.06	7.75	3.09
10.0 mm LS	1.35	10.13	3.92

Calculated leak index from GS1, GS2, and GS3 at 90.85 L/min showing the high sensitivity of the glycine sensors. HS, healthy state; LS, leak state.

Comparison of the performance of glycine and PVDF patch sensors

The experimental conditions (test rig, flow conditions, position of sensors, leak sizes, and sampling conditions) of the glycine validation was chosen to approximately replicate those of our previous validation of PVDF patch sensors for the same application,[26] with the only difference being that the leak introduction was not in real time in the case of the PVDF. This allows for a comparison between the performance of both sensor materials. Figure 5 shows a representative bar chart comparing the calculated leak index (explained in the preceding section) recorded by the sensors directly above the leak (i.e., the 60-cm mark from inlet), GS2, and PS2 at the flow rate of 71.92 L/min. The data show that for a worsening LS, the leak index increases for both sensors, but the leak index of the glycine sensor is consistently higher than that of the PVDF sensor. This is the case for the other two sensors and for all leak test scenarios. Although the PVDF patches have a higher piezoelectric strain constant (d_{33} = 18 pC/N) than the glycine patches (d_{33} = 0.9 pC/N), the low-dielectric constant (permittivity) of the glycine sensor means that it has a much lower capacitance (28 pF compared to the 3.30 nF of PVDF), and from the established strain-voltage relationships for piezoelectric patch sensors, the voltage output is inversely proportional to the capacitance. The capacitance of the fabricated glycine patch is orders of magnitude less than that of PVDF patches, so much so that the higher d_{33} of PVDF patches is negligible, and the voltage output of glycine is higher under similar strain conditions.

The relationship between the strain acting on the piezoelectric patch and the resulting voltage is presented as[37]

$$V_p = \frac{\varepsilon_1 S_q}{C_P}, \qquad \text{(Equation 1)}$$

where V_P represents the voltage generated by the sensor, ε_1 is the strain acting on the sensor, C_P is capacitance of the sensor, and S_q is a sensitivity parameter = $d_{ij}YA_p$. In addition, d_{ij} is the piezoelectric constant, Y is Young's modulus of the piezoelectric material, and A_p is the area of the sensor.

Leak localization based on attenuation mechanism of the NPW

After detection of the onset of a leak, the leak can be localized based on the mechanism of the leak-induced NPW decaying equally in both directions away from the leak position, consequently resulting in decreasing pipe surface vibration levels as one moves away from the leak. This localization can be achieved using amplitude and time-based analysis of the signals from the three glycine patch sensors bonded at varying distances from the leak.

Amplitude-based analysis

Figure 6 compares the recorded signals from all three glycine patch sensors, with each row of panels comparing the voltage signal output for three leak test scenarios

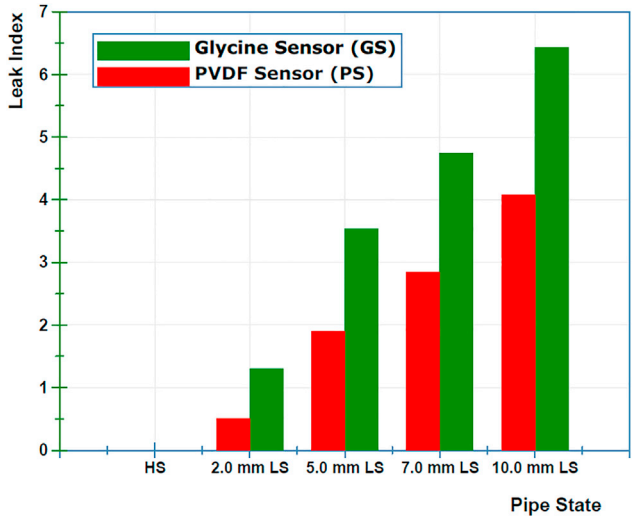

Figure 5. Device performance versus piezoelectric polymer patches
Comparison of leak index calculated for γ-glycine and PVDF sensors, GS2 and PS2 for the test scenarios at 71.92 L/min (19 gpm).

all having the same flow rate. Figures 6A–6C and 6D–6F present 3 leak test scenarios each at 71.92 L/min (19 gpm) and 26.50 L/min (7 gpm), respectively. The increase in the voltage signal is largest from GS2, while that of GS1 is the smallest for all leak test scenarios recorded. This is because GS2 is bonded along the test pipe at the same position as the leak (i.e., 60 cm from the pipe inlet) and records the maximum NPW-induced additional vibration. GS1 being furthest from the leak recorded the smallest additional vibration due to the continuous decay of the leak-induced NPW as it propagates away from the leak position.

These data demonstrate the potential of bio-piezoelectric sensors for real-world monitoring applications in complex pipe networks in, for example, municipal water supplies and underground oil transport. An array of piezoelectric patch sensors bonded to an extensive length of pipe can identify the onset, size, and location of a leak, opening the door to real-time monitoring using inexpensive, biocompatible materials with large potential benefits in waste reduction and minimization of environmental damage.

Time-based analysis

Amplitude-based analysis can localize the leak to a certain region, but it cannot report the exact position of the leak along the pipe length; for long pipe networks, a very dense coverage of sensors will raise the cost and complexity of the system. We show here that time-based analysis using the output from bio-crystal sensors can precisely pinpoint a leak position by triangulating the data from the spaced sensor and measuring the velocity of propagation of the NPW relative to one sensor upstream of a leak and another downstream. For any pipe health monitoring operation using vibration sensors, the sensor with the largest increase in the amplitude of its signal output due to a leak can be considered the one closest to the leak. Consequently, the nearest sensor upstream to that sensor will be a sensor upstream of the leak and similarly one downstream to that sensor, downstream of the leak. This can be used to identify the sensors whose output is to be considered in calculating the leak position.

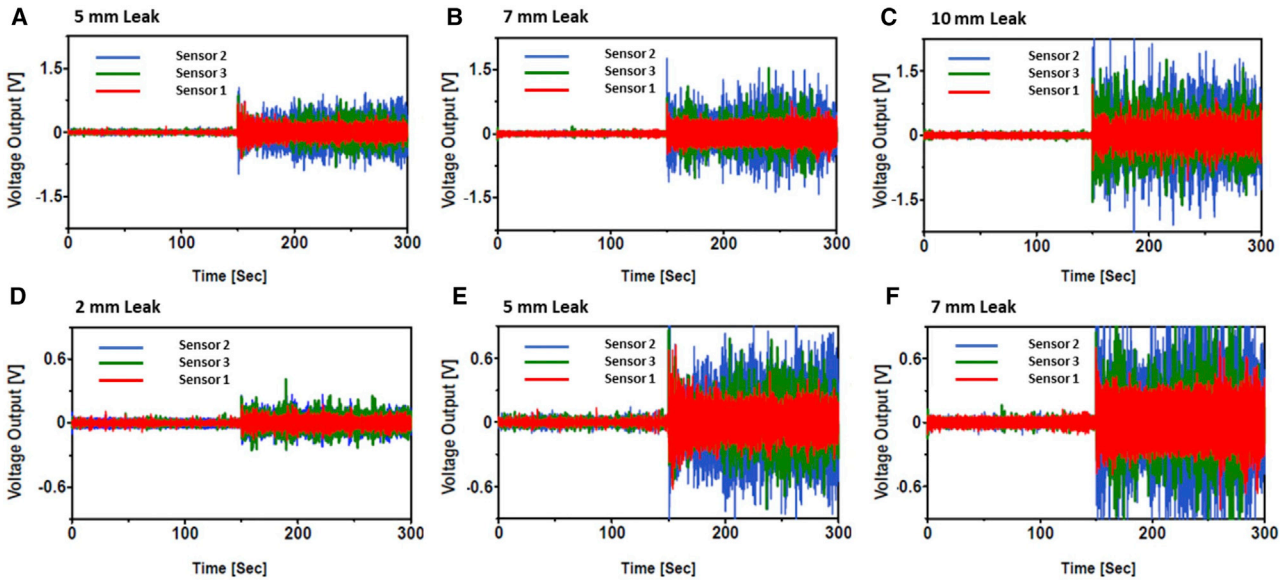

Figure 6. Amplitude-based analysis to determine leak location

(A–F) Voltage time plots for several leak test scenarios comparing sensor GS1 (red), GS2 (green), and GS3 (blue) outputs for a flow rate of 71.92 L/min for leak sizes of (A) 5 mm, (B) 7 mm, and (C) 10 mm leak size, and a flow rate of 26.50 L/min for leak sizes of (D) 2 mm, (E) 5 mm, and (F) 7 mm.

Applying this logic in the time-based analysis of data from this experiment, it can be seen from the recorded sensor output data that GS2 has the highest increase voltage amplitude of all leak test scenarios. As such, it is decidedly the sensor closest to the leak, and GS1 and GS3 are sensors upstream and downstream of the leak, respectively. This is consistent with what we know about the experimental setup. Hence, the leak can be localized by deducing the difference in travel time of the NPW to the positions of the pipe where GS1 and GS3 are bonded from the time series leak test scenarios' data recorded by these sensors. This time difference is $\Delta t = (t_1 - t_2)$, where t_1 is the time taken for the NPW to travel to position of GS1 and t_2 is the time taken to travel to GS3, respectively (see Figure S1).

Substituting the pipe properties shown in Table S1 and the density of water into Equation 11 in Note S3, the speed of travel of the NPW in the pipe was calculated to be 1.383 km/s. Knowing the position of the leak in this case and the speed of the NPW, the theoretical values of t_1, t_2, and $(t_1 - t_2)$ was calculated from Equations 16 and 17 in Note S4. This provides a benchmark for what can be expected as the experimental value of $(t_1 - t_2)$ from analyzing recorded leak data from GS1 and GS3. The theoretical value of $(t_1 - t_2)$ is calculated to be 1.46×10^{-4} s. In the experiment, the data sampling frequency in all test scenarios was 2 kHz, giving a period $1/f$ of 5×10^{-4} s. Although the NPW will travel to GS3 faster than to GS1, 1 time step of recorded data, which is same as the period of sampling (5×10^{-4} s), is greater than both the theoretical values of the travel times of the NPW to both sensors (t_1, and t_2) and the difference in these travel times ($t_1 - t_2$). As such, analysis of the recorded data is expected to show that the onset of a leak influences the output of both sensors GS1 and GS3 just 1 time step after leak introduction.

In analyzing the experimental data, the time series wavelet transform (WT) change-point detection algorithm was used to determine the point in time when an abrupt

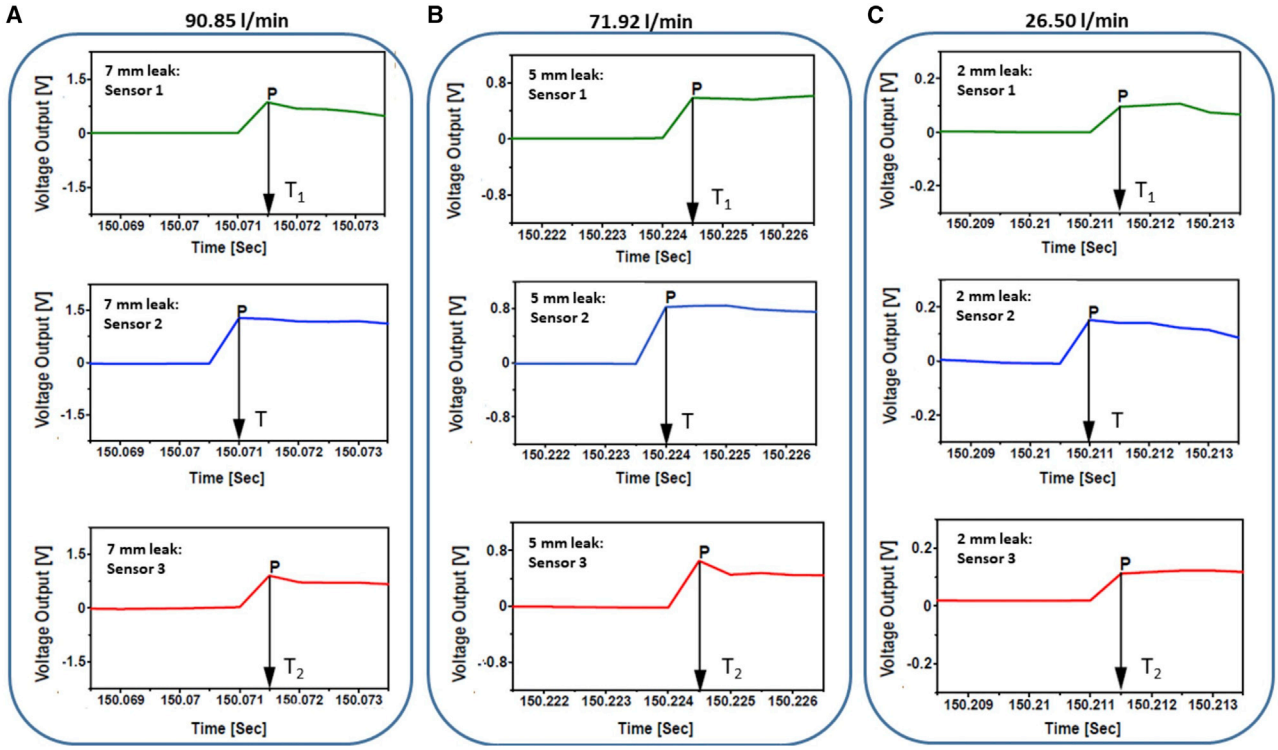

Figure 7. Time-based analysis to determine leak location

(A–C) Plots for 3 leak test scenarios, focusing in on the region of data at the time of leak introduction to show the abrupt change points for GS1, GS2, and GS3 and their coincident times T_1, T, and T_2 for leak sizes of (A) 7 mm with a flow rate of 90.95 L/min, (B) 5 mm with a flow rate of 71.92 L/min, and (C) 2 mm with a flow rate of 26.50 L/min, respectively.

Other figures present the full spectrum of data points sampled at 2,000 Hz/s for 5 min; for time-based analysis, only a handful of points just before and after the abrupt increase in output due to leak is required and thus plotted here.

increase in the time series signal output of the sensors was recorded. WT analysis is the most suitable for detecting discontinuity, singularity, and abrupt transitions in signals. It addresses transient variation detection by appropriately scaling up the signal to find the instantaneous/sharp transition.[45–50] Using this algorithm, T_1, T_2, and T were determined for all three sensors and all leak scenarios, T_1 being the change point for GS1, T_2 being the change point for GS3, and T being the change point for GS2. Since GS2 is bonded at the same position along the test pipe length as the leak, T was regarded as the time of instantaneous leak introduction and the absolute zero time in terms of propagation of the NPW. T_1 is the sum of the absolute zero time and the time it takes for the NPW to travel to GS1 (i.e., $(T + t_1)$). Similarly, T_2 is the sum of the absolute zero time and the time it takes for the NPW to travel to GS3 (i.e., $(T + t_2)$). Since

$$T_1 - T_2 = (T + t_1) - (T + t_2) = (t_1 - t_2),$$

$T_1 - T_2$ can be used as the time difference for the NPW to travel to positions of the pipe where GS1 and GS3 were bonded.

Figure 7 shows representative plots of all 3 sensor outputs in the leak data region, for 3 test case scenarios, identifying the change points T_1, T and T_2, recorded by GS1, GS2, and GS3, respectively. In Figure 7A, T is 150.071 s. Theoretically, it is expected that T_1 = 150.0302914 s and T_2 = 150.0301454 s, but since our sampling frequency is only as small as 5×10^{-4} s, the values of T_1 and T_2 obtained from analysis of the

experimental data is the same and equal to T plus 1 time step, which is equal to 150.0715 s. This trend is also observed in Figures 7B and 7C.

From these findings, we learn that to be able to use the output of the fabricated glycine patch sensors and indeed any piezoelectric patch sensor for time-based leak localization, the sampling frequency needs to be very high (much greater than 2 kHz) and/or the pipe being monitored must have a very long length, such that the sensors are bonded further away from one another. This will ensure that the time it takes the NPW to propagate to the upstream and downstream sensors is sufficiently larger than the sampling time. This is especially the case for metal pipes—the speed of propagation of NPW in them is very high (on the order of kilometers/second). Given that in practice for these applications, a sampling frequency of 2 kHz is considered sufficient and going higher may not be sustainable, it is safe to assert that time-based localization of leaks in metal pipes using the fabricated γ-glycine patch sensors and other piezoelectric patch sensors is only feasible for monitoring pipes that travel long distances (i.e., extensive pipe lengths).

These results demonstrate some key milestones in the field of piezoelectric sensing. While glycine has been a common test case in the validation and engineering of biological piezoelectrics,[11,12,51–53] up to now its device fabrication has consisted of placing[10,54] or printing crystals[55] between rigid electrodes and polymers.[56] This is the first validation of a thick, flexible, polycrystalline amino acid device component for real-time sensing with repeatable, reliable outputs that exceed the energy-harvesting properties of PVDF patches for such applications.

In this work, we demonstrate a simple fabrication method for the deposition of organic piezoelectric γ-glycine crystals on flexible conductive substrates for the fabrication of bio-based patch sensors for effective real-time environmental monitoring. The sensors demonstrate vibration-based real-time leak detection, monitoring, and localization in water pipes based on the leak-induced NPW and its propagation attenuation. The sensors are effective for leak detection in metal pipes and for continuous monitoring of a worsening leak condition over time. Amplitude-based signal analysis successfully locates the leak region, and time-based leak localization analysis demonstrates that the fabricated glycine sensors can localize leaks in metal pipes to an almost exact position along the pipe length. Time-based analysis is suitable for monitoring pipes that travel long distances due to the high speed of propagation of the NPW in metal pipes. This work represents the first demonstration of a biomolecular crystal sensor for real-time monitoring and opens up an extensive area of application. The work shows that the low permittivity property of glycine patches makes them ideal sensors for the target application and other vibration-based SHM applications. Future work includes developing isolation and packaging procedures for the water-soluble active layer.

EXPERIMENTAL PROCEDURES

Resource availability

Lead contact

Further information and requests for resources should be directed to and will be fulfilled by the lead contact, Dr. Sarah Guerin (sarah.guerin@ul.ie).

Materials availability

This study did not generate new unique reagents. The glycine powder is available from Sigma-Aldrich.

Data and code availability

All of the data associated with this study are included in the article and the Supplemental information. Additional information is available from the lead contact upon reasonable request.

Formation of the crystals

Crystals of γ-glycine were grown from a supersaturated aqueous solution. Glycine and sodium chloride (NaCl) were dissolved in ultrapure water in the ratio of 3:1, as recommended by Bhat and Dharmaprakash.[6] Monovalent salts have been shown to enhance γ-glycine nucleation via salt-glycine ordering in solution,[57] without crystallizing themselves. The concentration of glycine used was doubled from our previous work,[10] to 0.6 g/mL, to ensure a dense continuous polycrystalline film. The solution was heated to 50°C while constantly stirring until all of the solids had dissolved. The solution was then removed from the heat and immediately pipetted onto flexible copper tape (∼1 mL of solution per device). The solution was left to evaporate for 24 h in ambient conditions.

Optical microscopy

Optical images were taken using an Olympus BX51 Light Microscope connected to an Olympus SC50 Digital Camera.

XRD

XRD data were collected using a Panalytical Empyrean Diffractometer using Cu Kα radiation λ = 1.54060 Å. Diffraction patterns were collected in θ-2θ configuration at room temperature in the range of 15°–65° using a step size of 0.02°. Transmission XRD samples were prepared using Mylar polyester thin film sample supports.

Fabrication of sensor patches from the crystals

After growing crystals directly onto the bottom electrode of copper tape, a hard mask that prevents shorting between electrodes was used to place the top electrode (also adhesive copper tape from Radionics), similar to the method used by Hosseini et al.[56] Two wires were soldered onto each electrode on both sides of each glycine crystal film for taking away the generated charge.

The 6 glycine sensors fabricated were visually identical and labeled sensors A to F. The longitudinal piezoelectric constant, d_{33}, of these sensors was measured using a commercial d_{33} meter (Piezo Test), and the sensors were found to have piezoelectric constants of 0.9, 1.1, 0.9, 0.9, 1.2, and 0.5 pC/N, respectively.

For experimental testing, it was required that all sensors have same properties, so their outputs are comparable; hence, sensors A, C, and D were used in this work. Using a digital multimeter, the capacitance of these sensors was determined to be ∼28 pF.

Fabrication of leak plug

Leak plugs were used to introduce a pipe LS in real time. The leak was plugged and data from the sensors recorded under various flow conditions. After a chosen period of 150 s, the plugs were removed to initiate an instantaneous transition from a healthy pipe state to a leak pipe state.

Due to the unique requirements of these experiments, the leak plugs were designed in-house, with each leak plug tailored for a required leak size. The leak plugs have two sections: the ring section for handling and the rubber section for plugging the

leaks. A total of 4 leak plugs were fabricated with identical ring sections, printed from clear resin using a Stereolithography (SLA) 3-dimensional (3D) printer from Form Lab. After printing, the rings were washed in isopropanol and then cured using a Form Cure machine that uses both heat and 405 nm light for a fast and effective post-cure. Post-curing helps 3D-printed parts achieve successful burnout and results in the highest possible strength and stability.[58]

The rubber section was made from silicone cast in molds. The molds were 3D printed from clear resin. Platinum-catalyzed silicone "dragon skin" was selected as the plug rubber because of its flexibility and resilience.[59]

Dragon skin is a two-part silicone that requires mixing equal amounts of both parts. After measuring, the silicone was mixed in a planetary mixer. Before pouring the silicone into the molds, the molds were coated in a cure inhibition protection agent Inhibit X using appropriate safety measures. This agent stops platinum-catalyzed silicones from suffering from cure inhibition. A release agent was sprayed onto the molds to allow for easy detachment of the silicone rubbers after curing. After mixing and curing, the silicone was degassed under vacuum.

After curing, the silicone rubbers were removed from the molds. The silicone adhesive silpoxy was used to bond the rings and the plug rubbers together, with each leak plug having rubber sections to match the proposed pipe leak holes. For the experiment, leak holes of 2, 5, 7, and 10 mm diameters were introduced, and their corresponding leak plugs had rubber sections with 3, 6, 8, and 11 mm diameters, respectively. The extra 1 mm of each plug rubber section in comparison to the leak holes is to ensure they form an effective leak-proof seal when sandwiched into the leak hole to create a no-leak condition. The silicone rubber has a height of 3 mm, which is 0.5 mm more than the 2.5-mm thickness of the test pipe.

Test setup and procedure

With the fabricated glycine patches bonded on the test pipe section of the fluid test rig, the validation tests were conducted at 4 different flow rates of 90.85 L/min (24 gpm), 71.92 L/min (19 gpm), 45.42 L/min (12 gpm), and 26.50 L/min (7 gpm). The highest flow rate of 90.85 L/min was obtained when the pump was turned on with the test rig return valve completely shut. The other flow rates were achieved by opening the return valve to varying degrees, with the minimum flow rate of 26.50 L/min being the smallest required to keep the pipe filled with water. Baseline output from the sensors for the healthy pipe was first obtained from all 3 sensors by recording their output for 5 min for all 4 test flow rates after the fluid rig test pump was turned on and water was allowed to flow through the test pipe.

To validate the glycine patch sensors for real-time pipe leak detection and monitoring, a 2-mm diameter hole was introduced underneath GS2 at the 60-cm mark. This hole was plugged using the appropriate leak plug to restore the non-LS of the pipe. The test rig was turned on and data output from the sensors was recorded for 300 s for each of the test flow rate conditions, with the leak plug being pulled out each time after 150 s of data collection, initiating the transition from HS to LS.

The leak size was widened using the drill to make 5, 7, and 10 mm diameter leak holes, and with the aid of the appropriate leak plug, the same protocol was repeated for all leak conditions and test flow rates. The combination of the 5 pipe states (healthy pipe state and 4 leak pipe states) and the 4 flow rate conditions meant

that data from the glycine patch sensors were recorded for a total of 20 test scenarios (Table S2), with a given combination of a pipe state and a flow rate constituting a test scenario.

A three-channel charge amplifier was designed and fabricated for recording the sensor output, similar to that used previously.[36] The glycine patch sensors were connected through each channel of the charge amplifier to an NI-USB 6002 DAQ pad that records the sensor open circuit proportional voltage output signals. Using LabVIEW, the experiments were customized such that data sampling was done at a rate of 2 kHz for all of the test scenarios.

SUPPLEMENTAL INFORMATION

Supplemental information can be found online at https://doi.org/10.1016/j.xcrp.2021.100434.

ACKNOWLEDGMENTS

S.G. acknowledges support and funding from Science Foundation Ireland (SFI) under award number 12/RC/2275_P2. V.P. acknowledges support and funding from the Science Foundation Ireland MaREI Centre. F.O. acknowledges support and funding from the Irish Research Council and the Niger Delta Development Corporation.

AUTHOR CONTRIBUTIONS

F.O. carried out the fluid test rig experiments and analysis. S.G. grew and characterized the crystal-based sensors. F.O., S.G., and V.P conceptualized the project. M.C. supervised F.O. All of the authors contributed to writing the manuscript and data visualization.

DECLARATION OF INTERESTS

S.G. declares US Patent Application 16/606,127.

INCLUSION AND DIVERSITY

One or more of the authors of this article self-identify as a member of the LGBTQ+ community.

Received: January 26, 2021
Revised: March 25, 2021
Accepted: April 20, 2021
Published: May 11, 2021

REFERENCES

1. Chorsi, M.T., Curry, E.J., Chorsi, H.T., Das, R., Baroody, J., Purohit, P.K., Ilies, H., and Nguyen, T.D. (2019). Piezoelectric biomaterials for sensors and actuators. Adv. Mater. *31*, e1802084.

2. Guerin, S., Tofail, S.A., and Thompson, D. (2019). Organic piezoelectric materials: milestones and potential. NPG Asia Mater. *11*, 1–5.

3. Shin, D.-M., Hong, S.W., and Hwang, Y.-H. (2020). Recent advances in organic piezoelectric biomaterials for energy and biomedical applications. Nanomaterials (Basel) *10*, 123.

4. Panda, P., and Sahoo, B. (2015). PZT to lead free piezo ceramics: a review. Ferroelectrics *474*, 128–143.

5. Zhang, S., Xia, R., and Shrout, T.R. (2007). Lead-free piezoelectric ceramics vs. PZT? J. Electroceram. *19*, 251–257.

6. Bhat, M.N., and Dharmaprakash, S. (2002). Growth of nonlinear optical γ-glycine crystals. J. Cryst. Growth *236*, 376–380.

7. Hod, I., Mastai, Y., and Medina, D.D. (2011). Effect of solvents on the growth morphology of DL-alanine crystals. CrystEngComm *13*, 502–509.

8. Moitra, S., and Kar, T. (2010). Growth and characterization of L-valine-a nonlinear optical crystal. Crystal Research and Technology. J. Exp. Ind. Crystallogr. *45*, 70–74.

9. Vijayan, N., Rajasekaran, S., Bhagavannarayana, G., Ramesh Babu, R., Gopalakrishnan, R., Palanichamy, M., and Ramasamy, P. (2006). Growth and characterization of nonlinear optical amino

acid single crystal: L-alanine. Cryst. Growth Des. *6*, 2441–2445.

10. Guerin, S., Stapleton, A., Chovan, D., Mouras, R., Gleeson, M., McKeown, C., Noor, M.R., Silien, C., Rhen, F.M.F., Kholkin, A.L., et al. (2018). Control of piezoelectricity in amino acids by supramolecular packing. Nat. Mater. *17*, 180–186.

11. Heredia, A., Meunier, V., Bdikin, I.K., Gracio, J., Balke, N., Jesse, S., Tselev, A., Agarwal, P.K., Sumpter, B.G., and Kalinin, S.V. (2012). Nanoscale ferroelectricity in crystalline γ-glycine. Adv. Funct. Mater. *22*, 2996–3003.

12. Kumar, R.A., Vizhi, R.E., Vijayan, N., and Babu, D.R. (2011). Structural, dielectric and piezoelectric properties of nonlinear optical γ-glycine single crystals. Physica B Condens Matter *406*, 2594–2600.

13. Guerin, S., O'Donnell, J., Haq, E.U., McKeown, C., Silien, C., Rhen, F.M.F., Soulimane, T., Tofail, S.A.M., and Thompson, D. (2019). Racemic amino acid piezoelectric transducer. Phys. Rev. Lett. *122*, 047701.

14. Guerin, S., Tofail, S.A., and Thompson, D. (2018). Longitudinal Piezoelectricity in Orthorhombic Amino Acid Crystal Films. Cryst. Growth Des. *18*, 4844–4848.

15. Isakov, D., Petukhova, D., Vasilev, S., Nuraeva, A., Khazamov, T., Seyedhosseini, E., Zelenovskiy, P., Shur, V.Y., and Kholkin, A.L. (2014). In situ observation of the humidity controlled polymorphic phase transformation in glycine microcrystals. Cryst. Growth Des. *14*, 4138–4142.

16. Adegboye, M.A., Fung, W.-K., and Karnik, A. (2019). Recent advances in pipeline monitoring and oil leakage detection technologies: principles and approaches. Sensors (Basel) *19*, 2548.

17. Choi, J., Shin, J., Song, C., Han, S., and Park, D.I. (2017). Leak detection and location of water pipes using vibration sensors and modified ML prefilter. Sensors (Basel) *17*, 2104.

18. Gao, Y., Muggleton, J.M., Liu, Y., and Rustighi, E. (2017). An analytical model of ground surface vibration due to axisymmetric wave motion in buried fluid-filled pipes. J. Sound Vibrat. *395*, 142–159.

19. Zhang, Q., Wu, F., Yang, Z., Li, G., and Zuo, J. (2019). Simulation of the Transient Characteristics of Water Pipeline Leakage with Different Bending Angles. Water *11*, 1871.

20. El-Zahab, S., Abdelkader, E.M., and Zayed, T. (2018). An accelerometer-based leak detection system. Mech. Syst. Signal Process. *108*, 276–291.

21. Gao, Y., Brennan, M.J., Joseph, P., Muggleton, J., and Hunaidi, O. (2005). On the selection of acoustic/vibration sensors for leak detection in plastic water pipes. J. Sound Vibrat. *283*, 927–941.

22. Ismail, M., Dziyauddin, R.A., and Salleh, N.A.A. (2015). Performance evaluation of wireless accelerometer sensor for water pipeline leakage. In In Proceedings of the 2015 IEEE International Symposium on Robotics and Intelligent Sensors (IRIS) (IEEE), pp. 120–125.

23. Varanis, M., Silva, A., Mereles, A., and Pederiva, R. (2018). MEMS accelerometers for mechanical vibrations analysis: a comprehensive review with applications. J. Braz. Soc. Mech. Sci. Eng. *40*, 527.

24. Wang, Y.-H., Song, P., Li, X., Ru, C., Ferrari, G., Balasubramanian, P., Amabili, M., Sun, Y., and Liu, X. (2018). A paper-based piezoelectric accelerometer. Micromachines (Basel) *9*, 19.

25. Mahmood, M.S., Celik-Butler, Z., and Butler, D.P. (2017). Design, fabrication and characterization of flexible MEMS accelerometer using multi-Level UV-LIGA. Sens. Actuators A Phys. *263*, 530–541.

26. Okosun, F., Cahill, P., Hazra, B., and Pakrashi, V. (2019). Vibration-based leak detection and monitoring of water pipes using output-only piezoelectric sensors. Eur. Phys. J. Spec. Top. *228*, 1659–1675.

27. Kim, H., Torres, F., Wu, Y., Villagran, D., Lin, Y., and Tseng, T.-L.B. (2017). Integrated 3D printing and corona poling process of PVDF piezoelectric films for pressure sensor application. Smart Mater. Struct. *26*, 085027.

28. Lee, C., and Tarbutton, J.A. (2014). Electric poling-assisted additive manufacturing process for PVDF polymer-based piezoelectric device applications. Smart Mater. Struct. *23*, 095044.

29. Hou, Q., Ren, L., Jiao, W., Zou, P., and Song, G. (2013). An improved negative pressure wave method for natural gas pipeline leak location using FBG based strain sensor and wavelet transform. Math. Probl. Eng. *2013*, 278794.

30. Keramat, A., Tijsseling, A., Hou, Q., and Ahmadi, A. (2012). Fluid–structure interaction with pipe-wall viscoelasticity during water hammer. J. Fluids Structures *28*, 434–455.

31. Li, S., Karney, B.W., and Liu, G. (2015). FSI research in pipeline systems–a review of the literature. J. Fluids Structures *57*, 277–297.

32. Tian, C.H., Yan, J.C., Huang, J., Wang, Y., Kim, D.-S., and Yi, T. (2012). Negative pressure wave based pipeline leak detection: challenges and algorithms. In In Proceedings of the 2012 IEEE International Conference on Service Operations and Logistics, and Informatics (SOLI) (IEEE), pp. 372–376.

33. Tijsseling, A. (1996). Fluid-structure interaction in liquid-filled pipe systems: a review. J. Fluids Structures *10*, 109–146.

34. Zhang, T., Tan, Y., Zhang, X., and Zhao, J. (2015). A novel hybrid technique for leak detection and location in straight pipelines. J. Loss Prev. Process Ind. *35*, 157–168.

35. Gama, A., Lannes, D., and Velandia, E. (2015). A piezoelectric strain transducer to evaluate the severity of pipe vibration. Exp. Tech. *39*, 70–77.

36. Okosun, F., Celikin, M., and Pakrashi, V. (2020). A Numerical Model for Experimental Designs of Vibration-Based Leak Detection and Monitoring of Water Pipes Using Piezoelectric Patches. Sensors (Basel) *20*, 6708.

37. Yazdekhasti, S., Piratla, K.R., Atamturktur, S., and Khan, A. (2018). Experimental evaluation of a vibration-based leak detection technique for water pipelines. Struct. Infrastruct. Eng. *14*, 46–55.

38. Lannes, D.P., Gama, A.L., and Bento, T.F.B. (2018). Measurement of flow rate using straight pipes and pipe bends with integrated piezoelectric sensors. Flow Meas. Instrum. *60*, 208–216.

39. Medeiros, K.A.R., de Oliveira, F.L.A., Barbosa, C.R.H., and de Oliveira, E.C. (2016). Optimization of flow rate measurement using piezoelectric accelerometers: application in water industry. Measurement *91*, 576–581.

40. He, G., Liang, Y., Li, Y., Wu, M., Sun, L., Xie, C., and Li, F. (2017). A method for simulating the entire leaking process and calculating the liquid leakage volume of a damaged pressurized pipeline. J. Hazard. Mater. *332*, 19–32.

41. Jia, Z.g., Ren, L., Li, H.n., Ho, S.C., and Song, G.b. (2015). Experimental study of pipeline leak detection based on hoop strain measurement. Struct. Contr. Health Monit. *22*, 799–812.

42. Peter, M.E., and Ramasamy, P. (2010). Growth of gamma glycine crystal and its characterisation. Spectrochim. Acta A Mol. Biomol. Spectrosc. *75*, 1417–1421.

43. Wei, Y., and Xu, Q. (2015). An overview of micro-force sensing techniques. Sens. Actuators A Phys. *234*, 359–374.

44. Roscow, J., Lewis, R., Taylor, J., and Bowen, C. (2017). Modelling and fabrication of porous sandwich layer barium titanate with improved piezoelectric energy harvesting figures of merit. Acta Mater. *128*, 207–217.

45. Aminikhanghahi, S., and Cook, D.J. (2017). A survey of methods for time series change point detection. Knowl. Inf. Syst. *51*, 339–367.

46. Christodoulou, S.E., Kourti, E., and Agathokleous, A. (2017). Waterloss detection in water distribution networks using wavelet change-point detection. Water Resour. Manage. *31*, 979–994.

47. Lu, X., Sang, Y., Zhang, J., and Fan, Y. (2006). A pipeline leakage detection technology based on wavelet transform theory. In In Proceedings of the 2006 IEEE International Conference on Information Acquisition (IEEE), pp. 1432–1437.

48. Rashid, S., Qaisar, S., Saeed, H., and Felemban, E. (2014). A method for distributed pipeline burst and leakage detection in wireless sensor networks using transform analysis. Int. J. Distrib. Sens. Netw. *10*, 939657.

49. Srirangarajan, S., Allen, M., Preis, A., Iqbal, M., Lim, H.B., and Whittle, A.J. (2013). Wavelet-based burst event detection and localization in water distribution systems. J. Signal Process. Syst. Signal Image Video Technol. *72*, 1–16.

50. Taghvaei, M., Beck, S., and Staszewski, W. (2007). Leak detection in pipeline networks using low-profile piezoceramic transducers. Struct. Control Health Monit. *14*, 1063–1082.

51. Bishara, H., Nagel, A., Levanon, M., and Berger, S. (2020). Amino acids nanocrystals for piezoelectric detection of ultra-low mechanical pressure. Mater. Sci. Eng. C *108*, 110468.

52. Isakov, D., Gomes, E.M., Bdikin, I., Almeida, B., Belsley, M., Costa, M., Rodrigues, V., and Heredia, A. (2011). Production of polar βglycine nanofibers with enhanced nonlinear optical

and piezoelectric properties. Cryst. Growth Des. *11*, 4288–4291.

53. Seyedhosseini, E., Ivanov, M., Bystrov, V., Bdikin, I., Zelenovskiy, P., Shur, V.Y., Kudryavtsev, A., Mishina, E.D., Sigov, A.S., and Kholkin, A.L. (2014). Growth and nonlinear optical properties of β-glycine crystals grown on Pt substrates. Cryst. Growth Des. *14*, 2831–2837.

54. Hosseini, E.S., Manjakkal, L., and Dahiya, R. (2018). Bio-organic glycine based flexible piezoelectric stress sensor for wound monitoring. In In Proceedings of the 2018 IEEE Sensors (IEEE), pp. 1–4.

55. Slabov, V., Vasileva, D., Keller, K., Vasilev, S., Zelenovskiy, P., Kopyl, S., Shur, V.Y., Vinogradov, A., and Kholkin, A.L. (2019). Controlled Growth of Stable beta-Glycine via Inkjet Printing. Cryst. Growth Des. *19*, 3869–3875.

56. Hosseini, E.S., Manjakkal, L., Shakthivel, D., and Dahiya, R. (2020). Glycine–chitosan-based flexible biodegradable piezoelectric pressure sensor. ACS Appl. Mater. Interfaces *12*, 9008–9016.

57. Han, G., Chow, P.S., and Tan, R.B. (2016). Effects of common inorganic salts on glycine polymorphic transformation: an insight into salt-dependent polymorphic selectivity. Cryst. Growth Des. *16*, 6499–6505.

58. Uzcategui, A.C., Muralidharan, A., Ferguson, V.L., Bryant, S.J., and McLeod, R.R. (2018). Understanding and improving mechanical properties in 3D printed parts using a dual-cure acrylate-based resin for stereolithography. Adv. Eng. Mater. *20*, 1800876.

59. Park, S., Mondal, K., Treadway, R.M., 3rd, Kumar, V., Ma, S., Holbery, J.D., and Dickey, M.D. (2018). Silicones for stretchable and durable soft devices: beyond sylgard-184. ACS Appl. Mater. Interfaces *10*, 11261–11268.